

Revealing the Local Cosmic Web from Galaxies by Deep Learning

SUNGWOOK E. HONG (홍성욱)^{1,2}, DONGHUI JEONG³, HO SEONG HWANG^{4,2} AND JUHAN KIM⁵

¹*Natural Science Research Institute, University of Seoul, 163 Seoulsiripdaero, Dongdaemun-gu, Seoul, 02504, Republic of Korea*

²*Korea Astronomy and Space Science Institute, 776 Daedeokdae-ro, Yuseong-gu, Daejeon 34055, Republic of Korea*

³*Department of Astronomy and Astrophysics, and Institute for Gravitation and the Cosmos, The Pennsylvania State University, University Park, PA 16802, USA*

⁴*Astronomy Program, Department of Physics and Astronomy, Seoul National University, 1 Gwanak-ro, Gwanak-gu, Seoul 08826, Republic of Korea*

⁵*Center for Advanced Computation, Korea Institute for Advanced Study, 85 Heogiro, Dongdaemun-gu, Seoul, 02455, Republic of Korea*

ABSTRACT

The 80% of the matter in the Universe is in the form of dark matter that comprises the skeleton of the large-scale structure called the Cosmic Web. As the Cosmic Web dictates the motion of all matter in galaxies and inter-galactic media through gravity, knowing the distribution of dark matter is essential for studying the large-scale structure. However, the Cosmic Web's detailed structure is unknown because it is dominated by dark matter and warm-hot inter-galactic media, both of which are hard to trace. Here we show that we can reconstruct the Cosmic Web from the galaxy distribution using the convolutional-neural-network-based deep-learning algorithm. We find the mapping between the position and velocity of galaxies and the Cosmic Web using the results of the state-of-the-art cosmological galaxy simulations, *Illustris-TNG*. We confirm the mapping by applying it to the *EAGLE* simulation. Finally, using the local galaxy sample from *Cosmicflows-3*, we find the dark-matter map in the local Universe. We anticipate that the local dark-matter map will illuminate the studies of the nature of dark matter and the formation and evolution of the Local Group. High-resolution simulations and precise distance measurements to local galaxies will improve the accuracy of the dark-matter map.

Keywords: Local Group; dark matter; large-scale structure of universe

1. INTRODUCTION

Since Fritz Zwicky inferred its existence from the large velocity dispersion of the Coma cluster (Zwicky 1933) and Vera Rubin confirmed it with the flat rotation curve of galaxies (Rubin & Ford 1970), astronomers have been only strengthening the necessity of the non-baryonic matter providing excess gravity. We call that dark matter. The most substantial pieces of evidence include an excessive mass-to-light ratio in the dwarf galaxies (Aaronsen 1983), the mismatch between the X-ray map (gas distribution) and the weak gravitational lensing map (mass distribution; Clowe et al. 2006), as well as the disparity between the heights of even- and odd-acoustic peaks in the temperature power spectrum of the cosmic microwave background (Larson et al. 2011). Dark matter is also an indispensable component of the con-

dance cosmological model. Accounting for the measured expansion rate of the Universe (Planck Collaboration et al. 2018) requires the matter component whose energy density is over five times larger than that of atoms for which the robust upper limit comes from big-bang nucleosynthesis (Cooke et al. 2014). The observed large-scale distribution of galaxies (Anderson et al. 2014) and the map of weak-gravitational lensing potential (Abbott et al. 2018) also require the dark matter providing the skeleton of the large-scale structure within which clouds of atoms collapse to form stars and galaxies (Davis et al. 1985).

With the essential role that dark matter plays in modern astronomy and cosmology, in the past few decades, there have been continuous efforts to search for the nature of dark-matter *particles* in the particle accelerators (Atlas Collaboration 2019; Vannerom 2019), cosmic rays (Giesen et al. 2015), gamma-rays (Ackermann et al. 2015), and high-energy neutrinos (Aartsen et al. 2018). Beyond the Milky-way halo, there have also

been recent studies focusing on the dark-matter signals from the extra-galactic sources by cross-correlating the high-energy cosmic rays with the distribution of galaxies (Fornasa et al. 2016; Fang et al. 2020) and dark matter traced by weak-gravitational lensing (Tröster et al. 2017; Ammazalorso et al. 2020). All searches for the dark matter particles thus far, however, have not concluded with a firm detection. They have been only narrowing down the possible dark-matter masses and the interaction strengths among dark matter particles as well as between dark matter and atoms (Akerib et al. 2017; Arcadi et al. 2018). For these efforts of searching for the nature of dark matter, the most basic information currently lacking is the distribution of the dark matter, or Cosmic Web, in the local large-scale structure beyond the Milky-way halo. Of course, we have a good reason to believe that dark-matter halos surround each galaxy in the Universe. It is, however, also well known that the galaxies are biased, rather than faithful, tracers of the large-scale structure (Desjacques et al. 2018).

In this article, we shall present a novel method of unveiling the Cosmic Web in the local Universe. As dark matter is dark, of course, we cannot observe them directly from the telescope. The only guaranteed way of searching for the dark matter is the same method for their discovery, through their gravitational influence on visible objects. On the inter-galactic scales, dark matter dominates the gravitational interaction and determines the cosmic velocity flow. We can, therefore, infer the distribution of dark matter by carefully studying the distribution and motion of galaxies. Taking the observed distribution of galaxies and their peculiar velocity flow, in what follows, we shall decipher the dark matter distribution, or Cosmic Web, within local ~ 20 Mpc/ h .

When reconstructing the local dark-matter distribution directly from observed galaxy distributions, we face the following challenges. First, the local galaxy distribution at the low Galactic latitudes is hidden behind the intense radiation from the Galactic disk and contaminated by the interstellar gas and dust, which makes it hard to obtain the complete map of the galaxy distribution. Second, even if we had the complete map of galaxies, they are biased tracers of the large-scale structure; that is, the distribution of galaxies does not necessarily reflect the distribution of dark matter.

Previous attempts (Gottloeber et al. 2010; Libeskind et al. 2010; Carrick et al. 2015; Lavaux & Jasche 2016; Carlesi et al. 2016) of making the local dark-matter map, therefore, have relied on the cosmological simulations constrained by the smoothed density field at high-Galactic latitudes. Typically, a smoothing scale of a few Mpc is employed when matching the simulation

output to the observation. However, this observational constraint for the fully evolved galaxy distribution is non-trivial to implement because the simulation needs the density distribution at the initial time. Alternatively, the *Bayesian Origin Reconstruction from Galaxies* (BORG; see, e.g., Jasche & Wandelt 2013; Jasche et al. 2015) approach uses the multiple Gaussian processes to draw the probability distribution of the initial density perturbation from a given galaxy distribution. As based on the dark-matter density field evolution by second-order Lagrangian perturbation theory (2LPT) and linear galaxy bias model, the method is also limited to, again, the scale larger than a few Mpc where the 2LPT and linear bias models are accurate.

Here we overcome the challenges by taking a novel approach based on deep learning (DL). DL, as well as a conventional machine learning technique, has been introduced to measure the dark matter distribution from weak gravitational lensing or spatial distribution of dark matter halos (e.g., Modi et al. 2018; Shirasaki et al. 2019; Jeffrey et al. 2020). On the contrary, our DL approach aims to reconstruct the local dark-matter map down to an Mpc-scale by incorporating *all* information in the observed galaxy data: the spatial distribution and the radial peculiar velocity of galaxies. We use the convolutional neural network (CNN)-based DL algorithm to find the mapping between the local dark-matter distribution and the observed positions and the radial peculiar velocities of local galaxies.

The structure of this paper is as follows. In Section 2, we describe the simulation and observational data used for DL training and prediction, respectively. In Section 3, we will briefly describe our DL architecture and the evaluation of our DL model. In Section 4, we will show the reconstructed local dark matter map and its statistical robustness. We will summarize our result in Section 5.

Throughout the paper, we assume a standard Λ CDM cosmology in concordance with the *Planck* 2018 analysis (Planck Collaboration et al. 2018): $(\Omega_m^0, \Omega_\Lambda^0, h) = (0.31, 0.69, 0.6777)$. It is similar to the standard cosmologies adopted in *Illustris-TNG* and *EAGLE* simulations: $(\Omega_m^0, \Omega_\Lambda^0, h) = (0.3089, 0.6911, 0.6774)$ and $(0.307, 0.693, 0.6777)$, respectively (Springel et al. 2018; Schaye et al. 2015).

2. DATA

2.1. Observational Data: *Cosmicflows-3*

We use the *Cosmicflows-3* galaxy catalog (Tully et al. 2016, CF3 hereafter), one of the most comprehensive galaxy catalogs that provide distance, radial peculiar velocity, and luminosity of 17,647 galaxies up to 200 Mpc.

To produce a fair galaxy sample over the given region, we make the volume-limited sub-sample of the CF3 as follows. First, as the number density of the CF3 galaxies close to the Galactic plane (Galactic latitude $|b| < 10^\circ$) is lower than average, we only use the galaxies at $|b| > 10^\circ$. Also, we use the B -band absolute magnitude (M_B) compiled from *Lyon Extragalactic Database* (LEDA; Paturel et al. 2003) as a proxy of the stellar mass (M_* ; Wilman & Erwin 2012). We set the B -band magnitude -15 as the selection criterion, which is sufficient for covering the $20 \text{ Mpc}/h$ - and $40 \text{ Mpc}/h$ -cubic volume around the Milky-way galaxy. We have also tested the cases with $M_B < -16$ and -17 and found no noticeable difference of the predictions from the fiducial choice (see Section 4). Note that we have not used the K_S -band absolute magnitude, one of the best-known tracers of the stellar mass (Bell et al. 2003) because that information is missing for about 30% of the galaxies in our sample (Lavaux & Hudson 2011; Huchra et al. 2012).

We calculate the radial peculiar velocity by subtracting the Hubble flow from the velocity in the Galactic Standard of Rest (V_{GSR} ; Kourkchi et al. 2020). Note that we do not use the velocity in the cosmic microwave background (CMB) standard of rest (V_{CMB}) to reduce any bias that might be introduced in the conversion. Instead, when generating training and test samples from simulation data, we include the peculiar motion of the Milky-way corresponding galaxy in each simulation. There exists a difference on the Hubble constant between recent CMB observations ($H_0 = 67.77 \text{ km/s/Mpc}$; Planck Collaboration et al. 2018) and the best-fit from the CF3 ($H_0 = 75 \text{ km/s/Mpc}$; Tully et al. 2016). In this study, we have tested both values and find that the effect from the different Hubble constants stays within the uncertainty of the dark-matter map (see Section 4).

2.2. Simulation Data: Illustris-TNG & EAGLE

We use the TNG100-1, a simulation with a comoving volume $V = (75 \text{ Mpc}/h)^3$ and 1820^3 dark-matter and gas particles from the *Illustris-TNG* simulation suite (Springel et al. 2018; Pillepich et al. 2018; Marinacci et al. 2018; Naiman et al. 2018; Nelson et al. 2018, 2019), as our high-resolution simulation data (TNG100 hereafter). To mimic the observation from the Milky-way galaxy, we select 988 galaxies with stellar mass $4 \times 10^{10} M_\odot < M_* < 10^{11} M_\odot$ (*center galaxies* hereafter) by adopting that the Galactic stellar mass is about $5.2 \times 10^{10} M_\odot$ (Licquia & Newman 2015). Around each center galaxy, we make a sub-cube with $20 \text{ Mpc}/h$ box-size and calculate the dark-matter density field within the 64^3 uniform grid. We also calculate the relative position of galaxies with $M_B < -15$ (*target galaxies* here-

after) and the difference of peculiar velocity between the target galaxy and center galaxy.

For the low-resolution dark-matter map with $V = (40 \text{ Mpc}/h)^3$, we use the TNG300-1 from the *Illustris-TNG* simulations, whose volume and number of particles are $V = (205 \text{ Mpc}/h)^3$ and 2500^3 , respectively (TNG300 hereafter). Note that the amplitude of the luminosity function of TNG300 is lower than the observation and TNG100, mainly due to the lower spatial resolution of the simulation (Pillepich et al. 2018). Therefore, we also apply the *resolution correction* to find the center and target galaxies using the number density obtained from TNG100 rather than directly using the face values of M_* or M_B . We also use the TNG300-1-Dark, a dark-matter-only counterpart of the TNG300, to test how baryonic physics affects our result. We select the center and target galaxies by finding the mass cut of dark matter halos with the same number density. The result from the TNG300-1-Dark is similar to or slightly worse than TNG300 (see Section 4).

Also, we use the RefL0100N1504, a reference simulation with $V = (67.77 \text{ Mpc}/h)^3$ and 1504^3 dark-matter and gas particles from the *EAGLE* simulation suite (Schaye et al. 2015; Crain et al. 2015, *EAGLE* hereafter), to check the fidelity of our result. For the center galaxies, we use the same selection criterion to TNG100 and find 478 center galaxies. For the target galaxies, however, we do not directly use M_B . It is because the luminosity function of *EAGLE* is reliable only for bright galaxies ($M_B \lesssim -18$) since the *EAGLE* simulations calculate the luminosity only to massive galaxies ($M_* \geq 10^{8.5} M_\odot$; Camps et al. 2018). Instead, similar to TNG300, we use the galaxy number density obtained from TNG100 to find the stellar mass cut of target galaxies.

3. METHODS

3.1. Deep Learning Architecture

We construct the deep learning architecture using convolutional neural network (CNN) that highlights features in the data by a series of convolutions, resulting in so-called hidden layers. By varying the convolution filters, one can extract different physical features in the data. Specifically, we use a CNN architecture similar to the U-Net (Ronneberger et al. 2015) or V-Net (Milletari et al. 2016) to predict the dark-matter density field from the galaxy position and radial peculiar velocity (see Figure 1). Our CNN architecture consists of the following two stages: the encoding stage (Input-Conv N_s) with increasing number of filters and decreasing the size of hidden layers, and the decoding stage (UpConv N_s -Output) with decreasing number of filters and increasing the size of hidden layers. Here, N_s denotes the spatial size of

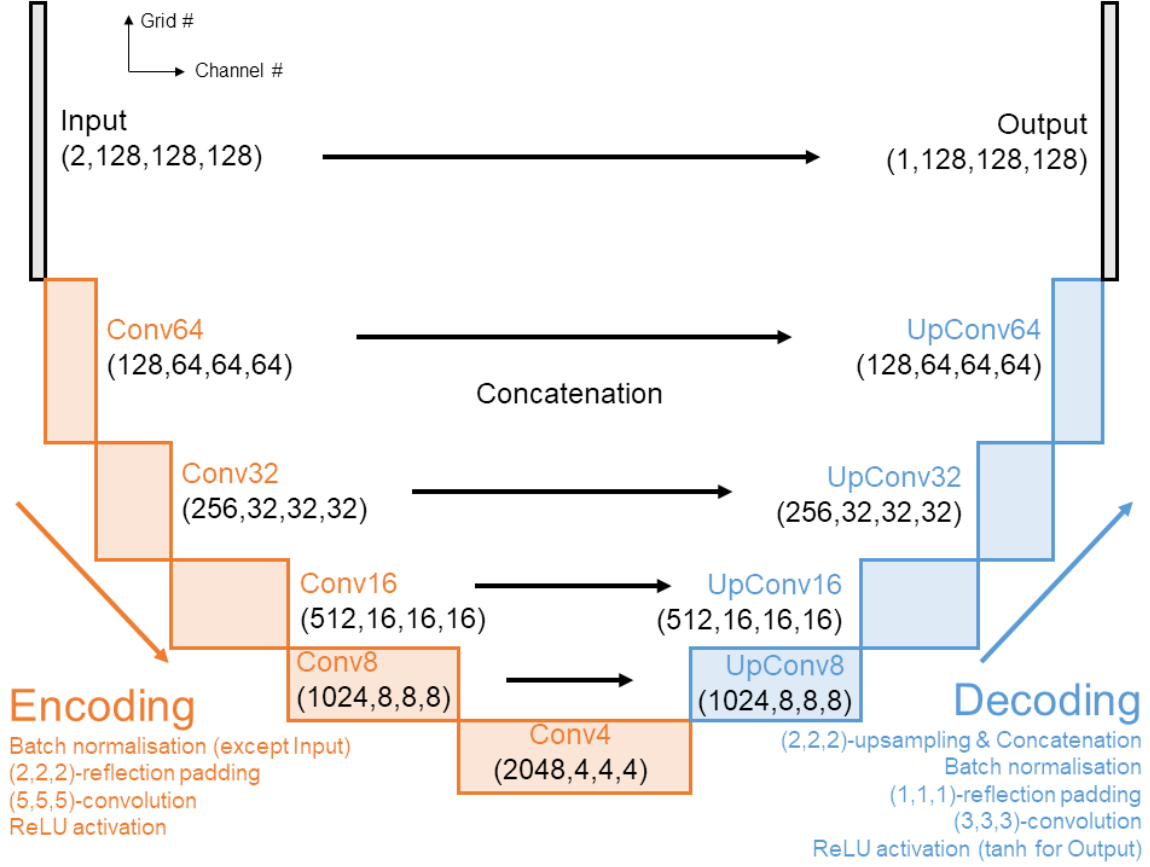


Figure 1. The convolutional neural network (CNN) architecture used for TNG300. We denote the layer size by the quadruple where the spatial dimension ($2^n, 2^n, 2^n$) follows the number of channels. The size (except the number of filters) of each layer for TNG100 is the half of TNG300.

hidden layers. To retain the small-scale spatial resolution, we also attach the hidden layers in the equivalent (with the same layer size) encoding stage as additional channels to the decoding layer, doubling the number of channels. We refer this process as concatenation.

The encoding stage consists of a series of $\text{Conv}N_s$ layers. Let us define the input of a given $\text{Conv}N_{s,0}$ as $\mathbb{I}_{\ell;i,j,k}$, where $i, j, k \in [1, N_{s,0}]$ is the spatial coordinates, and $\ell \in [1, N_{\text{ch},0}]$ is the channel index with $N_{\text{ch},0}$ being the total number of channels. To accommodate the convolution at the edge, we have added the buffer around the input array (*padding* process). As we use $5 \times 5 \times 5$ convolution filter, it suffices to add $N_p = 2$ padding pixels at both edges of each dimension. We fill the padding pixels by reflecting the inner two pixels next to the edge pixels.

After the padding, we apply a three-dimensional convolution with a multi-channel filter $w_{\ell,\ell';i',j',k'}$ and bias b_ℓ , with indices $i', j', k' \in [1, N_k = 5]$, $\ell \in [1, N_{\text{ch},1}]$,

$\ell' \in [1, N_{\text{ch},0}]$, to obtain the output \mathbb{C} as

$$\mathbb{C}_{\ell;i,j,k} = b_\ell + \sum_{\ell',i',j',k'} \mathbb{P}^{\ell';s(i';i),s(j';j),s(k';k)} w_{\ell,\ell';i',j',k'}, \quad (1)$$

where $\mathbb{P}^{\ell';s(i';i),s(j';j),s(k';k)}$ is the input array after the padding. We sample the convolution sparsely $s(i';i) = i \times N_{\text{st}} + i'$, and reduce the spatial dimension by a factor of 2^3 at each step by choosing the spatial interval $N_{\text{st}} = 2$ (*strides* hereafter). Accompanying the reduction of spatial dimension, we increase the number of channels N_{ch} by a factor of 2 at each step of the convolution, from 128 ($\text{Conv}64$) to 2048 ($\text{Conv}4$). Note that the convolution filter $w_{\ell,\ell';i',j',k'}$ and bias b_ℓ are *trainable parameters* which we adjust for the training.

The padding and convolution processes are linear operations, so any combinations of these operations simplify to a single linear algebra operation. In order to fully utilize the multiple hidden layers of Deep Learning, we apply the rectified linear unit (ReLU; Hahnloser et al. 2000; Glorot et al. 2011),

$$\mathbb{A}_{\ell;i,j,k} = \max(\mathbb{C}_{\ell;i,j,k}, 0), \quad (2)$$

as a non-linear *activation function* for each hidden layer.

Finally, we apply the batch normalization (Ioffe & Szegedy 2015)

$$\mathbb{O}_{\ell;i,j,k} = \gamma_{\ell;i,j,k} \frac{\mathbb{A}_{\ell;i,j,k} - \mu_{\ell;i,j,k}}{\sigma_{\ell;i,j,k}^2 + \epsilon} + \beta_{\ell;i,j,k}, \quad (3)$$

to obtain an output $\text{Conv}N_{s,1}$ layer, $\mathbb{O}_{\ell;i,j,k}$ ($i, j, k \in [1, N_{s,1} = N_{s,0}/2]$, $\ell \in [1, N_{\text{ch},1}]$). Here, $\mu_{\ell;i,j,k}$ and $\sigma_{\ell;i,j,k}$ are the mean and standard deviation of $\mathbb{A}_{\ell;i,j,k}$ over samples in a same *mini-batch*, and $\epsilon = 10^{-3}$ is a small value for the numerical stability. Note that the mini-batch refers to the bundle of input-output pairs that we have used for updating the trainable parameters. The normalization factor $\gamma_{\ell;i,j,k}$ and bias factor $\beta_{\ell;i,j,k}$ are another trainable parameters. The batch normalization introduces extra level of non-linearity ensuring that the trainable parameters introduced at earlier hidden layers still affect the output.

The decoding stage consists of a series of $\text{UpConv}N_s$ layers, which are constructed in a parallel manner. In contrast to the $\text{Conv}N_s$, where we decreases the spatial dimension by sparsely sampling the convolved array, we increase the spatial dimension of each $\text{UpConv}N_s$ layer:

$$\mathbb{U}_{\ell;i,j,k} = \mathbb{I}_{\ell;u(i),u(j),u(k)}, \quad (4)$$

by duplicating the input array $\mathbb{I}_{\ell;i,j,k}$. Here, $u(x) = \lceil x/N_u \rceil$, and we set the upsampling factor $N_u = 2$ in order to increase the spatial size of $\mathbb{U}_{\ell;i,j,k}$ by a factor of 8. After the upsampling, we concatenate the $\text{Conv}N_s$ layer (the same size), and apply batch normalization. We then apply a three-dimensional convolution with $(N_k, N_{\text{st}}) = (3, 1)$, after the reflective padding the edge arrays with $N_p = 1$. We decrease the number of output channels of each $\text{UpConv}N_s$ from 1024 to 128 by a factor of 2. After the convolution, we apply the ReLU activation function.

In addition to the usual steps described above, the final **Output** layer requires following two special treatments so that the output layer represents the single dark-matter density proportional to $\log_{10}(\rho/\rho_0)$ which can be both positive and negative. First, instead of a gradual decrease of the number of output channels by a factor of 2, we set the number of output channels for **Output** as 1. Second, instead of the ReLU activation function, whose output range is $[0, +\infty)$, we use the hyperbolic tangent function (\tanh) so that its output range becomes finite ($[-1, +1]$ in this case).

We have adopted different spatial size of the hidden layer for TNG100 and TNG300 to accommodating the difference in their spatial resolution. For TNG100, the encoding stage starts from 2 channels of 64^3 -grid input layers, and ends with the 2,048 channels of the 2^3 -grid layer (**Conv2**), and, for TNG300, the encoding stage

starts from 2 channels of 128^3 -grid input layers, and ends with the 2,048 channels of the 4^3 -grid layer (**Conv2**). The final output layers are 64^3 and 128^3 for, respectively, TNG100 and TNG300. We have also tested other CNN architectures with various channel sizes, and confirmed that the CNN architecture that we use here (shown in Figure 1) performs the best among the tested cases.

3.2. Training

We divide the training and validation samples from TNG100 so that all sub-cubes from the validation sample do not overlap with those from the training sample. As a result, we only use 525 sub-cubes — 432 for training and 93 for validation. For each sub-cube, we make two 64^3 uniform grids as a two-channel input layer; each channel stores the number of target galaxies (N_{gal}) and the averaged radial peculiar velocity (V_{pec}) in units of km/s. For the input layer, we apply the same Galactic-latitude mask as the CF3 data (masking out $|b| < 10^\circ$). For the output layer, we normalize the logarithm of dark-matter density to be

$$y = \frac{1}{4.5} \log_{10}(\rho/\rho_0), \quad (5)$$

where ρ_0 is the mean dark matter density of the Universe so that all values in the output layer would be between -1 and $+1$.

For data augmentation, we allow swapping the (x, y, z) -axes of each sub-cube, which increases the number of samples by a factor of three. We further increase the sample size by flipping the axis direction, with which the number of samples increases eight times. Note that, unlike U-Net or V-Net, we do not split a single cube into multiple smaller cubes for data augmentation because that would change of the Galactic-latitude mask and the radial peculiar velocity. In the end, we obtain 10,368 and 2,232 samples, respectively, in training and validation sets.

We implement our CNN architecture in the *Keras* (Chollet et al. 2015) with the *Tensorflow* backend (Abadi et al. 2015) and perform the training with the *NVIDIA Tesla V100* graphic processing unit (GPU) with 16GB memory. We choose the mean squared error (MSE) as the loss function that the DL minimizes during the training:

$$\mathcal{L}_{\text{TNG100}} = \frac{1}{n} \sum_{i=1}^n (y_{i,\text{pred}} - y_{i,\text{truth}})^2 \quad (6)$$

$$= \frac{1}{n} \sum_{i=1}^n \left[\frac{1}{4.5} \log_{10}(\rho_{i,\text{pred}}/\rho_{i,\text{truth}}) \right]^2, \quad (7)$$

where the subscripts (i, pred) and (i, truth) are, respectively, the prediction and truth values of the y (defined in Eq. 5) at i -th grid.

Initially, we set the trainable parameters in the convolution filters (θ ; *parameter vector* hereafter) randomly. The training process for minimizing the loss function is done with 200 *epochs*, a unit process that updates the parameter vector from a subset of the train set and applies the updated parameter vector to a subset of the validation set. The parameter vector update process at each epoch consists of 1728 mini-batches. We set the mini-batch size as 6, mainly due to the GPU memory limit. For each mini-batch we numerically calculate the gradient of the loss function ($\nabla_{\theta}\mathcal{L}$) and update the parameter vector by the Adam optimizer (Kingma & Ba 2014),

$$\theta_t = \theta_{t-1} - \alpha \frac{\mathbf{m}_t / (1 - \beta_1^t)}{\sqrt{\mathbf{v}_t / (1 - \beta_2^t) + \epsilon}} \quad (8)$$

$$\mathbf{m}_t = \beta_1 \mathbf{m}_{t-1} + (1 - \beta_1) \nabla_{\theta} \mathcal{L}_t(\theta_{t-1}) \quad (9)$$

$$\mathbf{v}_t = \beta_2 \mathbf{v}_{t-1} + (1 - \beta_2) [\nabla_{\theta} \mathcal{L}_t(\theta_{t-1})]^2. \quad (10)$$

Here t is a mini-batch step number starting from zero, \mathbf{m}_t and \mathbf{v}_t are the first and second-moment vectors with initial values $\mathbf{m}_0 = \mathbf{v}_0 = \mathbf{0}$, $\beta_1 = 0.9$ and $\beta_2 = 0.999$ are exponential decay rates for moment estimates, and $\epsilon = 10^{-7}$ is a small value for the numerical stability. α is the *learning rate* that determines how fast one updates the parameter vector, and we set it as 10^{-3} . As a result, the training process for TNG100 takes about 73 hours for a single run.

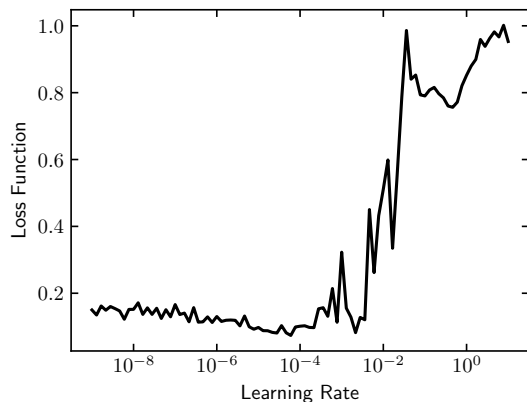


Figure 2. Evolution of loss function (\mathcal{L}) as a function of learning rate of Adam optimizer (α) from an additional test training for TNG300. Too low learning rate ($\alpha \lesssim 10^{-8}$) gives a too slow update of the parameter vector, which is presented as a flat slope of $\mathcal{L}(\alpha)$. On the other hand, too high learning rate ($\alpha \gtrsim 10^{-5}$) prevents finding a solution, which is presented as a noisy increment of $\mathcal{L}(\alpha)$.

We perform a similar training for the TNG300 outcome, except for the following differences. First, we have 10629 training sub-cubes and 1256 validation sub-cubes, with each sub-cube having 128^3 -grids. Unlike TNG100, we do not apply further data augmentation, mainly due to the expensive computational cost from large CNN architecture size. Second, since the dynamic range of dark-matter density of TNG300 is wider than TNG100, we use

$$y = \frac{1}{5} \log_{10}(\rho/\rho_0) \quad (11)$$

for the output layer instead. As a result, the MSE loss function becomes

$$\mathcal{L}_{\text{TNG300}} = \frac{1}{n} \sum_{i=1}^n \left[\frac{1}{5} \log_{10}(\rho_{i,\text{pred}}/\rho_{i,\text{truth}}) \right]^2. \quad (12)$$

Third, instead of using a fixed learning rate, we apply a triangular cyclic learning rate (Smith 2015),

$$\alpha_t = \alpha_L + \frac{\alpha_U - \alpha_L}{T/2} \times \min \{ (t \bmod T), T - (t \bmod T) \}, \quad (13)$$

to avoid the training to be stuck in local minima. Here T is the number of mini-batches that consists a single learning rate cycle, and we set it as 8. α_L and α_U are the minimum and maximum values of the learning rates, respectively. To find a suitable range of learning rates, we have performed an additional test training with a few epochs by varying learning rates (see Figure 2). If the learning rate is too low, i.e., if the parameter vector update is too slow, the loss function as a function of learning rate ($\mathcal{L}(\alpha)$) has a flat slope. On the other hand, if the learning rate is too high, i.e., if an interval of parameter vector update is too large to find a solution, $\mathcal{L}(\alpha)$ presents a noisy increment. We found that $3 \times 10^{-8} < \alpha < 4 \times 10^{-5}$ is a suitable range of the learning rate and set $(\alpha_L, \alpha_U) = (3 \times 10^{-8}, 4 \times 10^{-5})$ for the triangular cyclic learning rate accordingly. Finally, due to the large CNN architecture size, we use four *NVIDIA Tesla V100* GPUs with 32GB memory per each, with a mini-batch size of 8. For each training, we run 400 epochs by using only 157 mini-batches per epoch, and it takes about 90 hours for a single run.

Figure 3 shows the evolution of the MSE loss functions from both train and validation sets as a function of epoch in TNG300. Both train and validation losses similarly decrease over epoch until the validation loss reaches its minimum around 8×10^{-3} at ~ 140 epochs, while the train loss continues decreasing at all epochs. Similar minimum values of validation losses have been found during our test training, and we expect that the above value is close to the global minimum of the validation loss function in our current CNN setup. If the

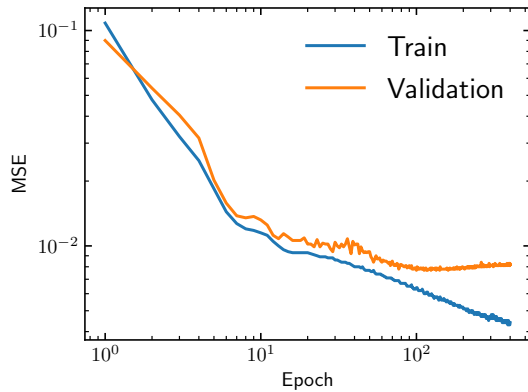


Figure 3. Evolution of loss functions from train (blue) and validation (orange) sets as a function of epoch for TNG300.

validation loss greatly increases over epoch after reaching its minimum while the train loss keeps decreasing, it may infer that the learning process starts overfitting the data—the learning process tries to memorize the data without finding any global feature. In our runs, however, the validation loss does not increase more than 1.1 times its minimum until the last epoch, which suggests that our result would not suffer from overfitting problem significantly. From each run, we select three models from three different epochs for the following performance test: at the minimum validation loss, at the minimum training loss, and the last epoch.

For TNG300, we perform six additional alternative training with different configurations of the input layer (*comparison models* hereafter) to understand how such difference affects our prediction (see Table 1). `16mag` and `17mag` use the alternative absolute B -band magnitude cutoffs $M_B < -16$ and -17 , respectively. `stellar-Mass` uses the logarithm of the total stellar mass rather than the simple galaxy number as an input layer, while `noVpec` does not use the radial peculiar velocity. Finally, `DMhalo` uses the dark matter halos in the dark-matter-only simulation TNG300-1-Dark instead of galaxies in the TNG300-1.¹

4. RESULTS

4.1. Performance Test

To test the model parameters tuned with TNG100 and TNG300 training sets, we apply the model to the validation samples to compare the resulting dark-matter density cube with the ground truth. Specifically, we

use the following four methods for the performance test—visual comparison, joint probability distribution, histogram, and two-point correlation function (2pCF) $\xi(r) = \langle \delta(\mathbf{x})\delta(\mathbf{x} + \mathbf{r}) \rangle_{\mathbf{x}}$. To examine the performance of the each model, we use the Kolmogorov-Smirnov statistics of the 2pCFs between truth and prediction at a given scale,

$$\text{KS}(\xi_{\text{pred}}, \xi_{\text{truth}}) = \max_{\xi'} |\tilde{P}_{\text{pred}}(\xi') - \tilde{P}_{\text{truth}}(\xi')|. \quad (14)$$

Here, $\tilde{P}(\xi') = N(\xi < \xi')/N_{\text{sample}}$ is the empirical distribution function, where N_{sample} and $N(\xi < \xi')$ are, respectively, the number of whole samples and the number of those satisfying $\xi < \xi'$. The smaller $\text{KS}(\xi_{\text{pred}}, \xi_{\text{truth}})$ indicates that the predicted probability distribution of the 2pCF is closer to the true distribution, so we use that as a metric to compare the performance of models. For both TNG100 and TNG300, the models at the minimum training loss provide the closest distribution of the 2pCF predictions to their truth, and we adopt them as our optimal models.

Table 2, Figures 4 and 5 show a visual inspection and the statistics of the TNG300 validation samples, which show a good agreement with their true values. Interestingly, the predicted dark matter distribution shows small-scale filamentary structures, which are not apparently shown in N_{gal} alone. This is the first indication of the importance of the (radial) peculiar velocity field for reconstructing the small-scale filamentary structures; that is, the recovered dark-matter map shows much more detailed structure than simply connecting the galaxy positions, since the peculiar velocity could provide information about the underlying gravitational potential. Simply put, we use the galaxies as test particles for recovering the local gravitational field. Note that, however, there is a slight difference in the detailed distribution of filamentary structures between truth and prediction. Also, note that there exists a sharp lower cut in the predicted density $\min \rho_{\text{pred}} \sim 10^{-2} \rho_0$. The above two issues could be overcome by using higher-resolution hydrodynamic simulations and observational data with more low-brightness galaxies. Also, fine-tuned choices of loss function might help manage an issue about a slight difference of filamentary structures.

After choosing the optimal models, we perform the convergence test between models with different simulation resolutions and setups. First, we compare the local dark-matter density field predictions from TNG100 and TNG300 within the radius $r = 10 \text{ Mpc}/h$. We find that they show similar distribution up to $r \sim 4 \text{ Mpc}/h$, while the dark-matter map from TNG100 shows finer small-scale structures than TNG300 (see Section 4.3). Also,

¹ Note that Modi et al. (2018) performed a similar study to reconstruct the (initial) density perturbation from the dark matter halo distributions by DL, while they focused more on large scales such as baryon acoustic oscillation (BAO) rather than relatively small scales such as ours.

Table 1. Summary of TNG300 and its comparison models used in this paper. Each comparison model is the same as TNG300 except those mentioned in its “Description.”

Model	Description
TNG300	Simulation: TNG300-1 hydrodynamic simulation. Center galaxies: $4 \times 10^{10} M_{\odot} < M_{\star} < 10^{11} M_{\odot}$ after resolution correction. Target galaxies: $M_B < -15$ after resolution correction. Input layer: 2-channel (N_{gal} and V_{pec}). Hubble parameter: 67.77km/s/Mpc
16mag	Target galaxies: $M_B < -16$ after resolution correction.
17mag	Target galaxies: $M_B < -17$ after resolution correction.
noVpec	Input layer: 1-channel (N_{gal}).
stellarMass	Input layer: 2-channel ($\log_{10}(M_{\star}/M_{\odot})$ (logarithm of the total stellar mass) and V_{pec}).
DMhalo	Simulation: TNG300-1-Dark dark-matter-only simulation. Center & target galaxies: applying halo mass cut that matches the same galaxy number density to TNG300.
diffH0	Hubble parameter: 75km/s/Mpc

Table 2. Summary of the performance test done by validation samples of TNG100, TNG300, and their comparison models. $\text{KS}(\xi_{\text{pred}}, \xi_{\text{truth}})$ is the Kolmogorov-Smirnov statistics of the two-point correlation functions of dark-matter distribution between truth and prediction. EAGLE-TNG100 is the application of the TNG100 model to the EAGLE samples. diffH0 is identical to TNG300 since Hubble flow estimation is not considered in this test.

Model	$\log_{10}(\rho_{\text{pred}}/\rho_{\text{truth}})$	$\text{KS}(\xi_{\text{pred}}, \xi_{\text{truth}})$		
		0 – 1 Mpc/h	1 – 3 Mpc/h	3 – 10 Mpc/h
TNG100	-0.014 ± 0.543	0.263 ± 0.035	0.175 ± 0.087	0.130 ± 0.042
EAGLE-TNG100	$+0.129 \pm 0.491$	0.171 ± 0.055	0.152 ± 0.047	0.149 ± 0.040
TNG300	-0.020 ± 0.451	0.153 ± 0.035	0.134 ± 0.040	0.163 ± 0.017
16mag	-0.008 ± 0.468	0.109 ± 0.010	0.161 ± 0.033	0.254 ± 0.016
17mag	$+0.017 \pm 0.481$	0.143 ± 0.037	0.168 ± 0.018	0.251 ± 0.019
noVpec	$+0.016 \pm 0.481$	0.367 ± 0.115	0.407 ± 0.061	0.170 ± 0.036
stellarMass	-0.050 ± 0.471	0.186 ± 0.056	0.218 ± 0.016	0.269 ± 0.021
DMhalo	$+0.002 \pm 0.481$	0.264 ± 0.029	0.243 ± 0.030	0.263 ± 0.034

we apply the CNN model from TNG100 to the test sample of EAGLE (EAGLE-TNG100 in Table 2).

Note that we do not apply the CNN model from TNG300 to EAGLE because the volume of EAGLE is not sufficiently larger than the volume of TNG300 sub-cubes. We find that its performance test result is similar to the TNG100 validation sample, except that EAGLE-TNG100 tends to slightly overestimate the dark-matter density (see Figure 5 and Table 2).

We also test the performance of various comparison models of TNG300 (see Table 1 for definitions). Most comparison models show similar overall performance to TNG300, while those from the dark-matter-only simula-

tion (DMhalo) has slightly more offset in the distribution of 2pCFs. Those without using the radial peculiar velocity as inputs (noVpec), however, do not reproduce any small-scale filamentary structure shown in the true dark matter distribution (see the right panel of Figure 4). From its visual inspection, one could interpret the output of noVpec as a smoothing of the galaxy number distribution—the only available input of the given DL model—with a few Mpc-scale. As a result, the 2pCFs of noVpec show a significant deviation from their truth in small scales with $r \lesssim 3 \text{ Mpc}/h$ (see Table 2). From the comparison to TNG300 and its other comparison models, it is apparent that the (radial) peculiar velocity plays a

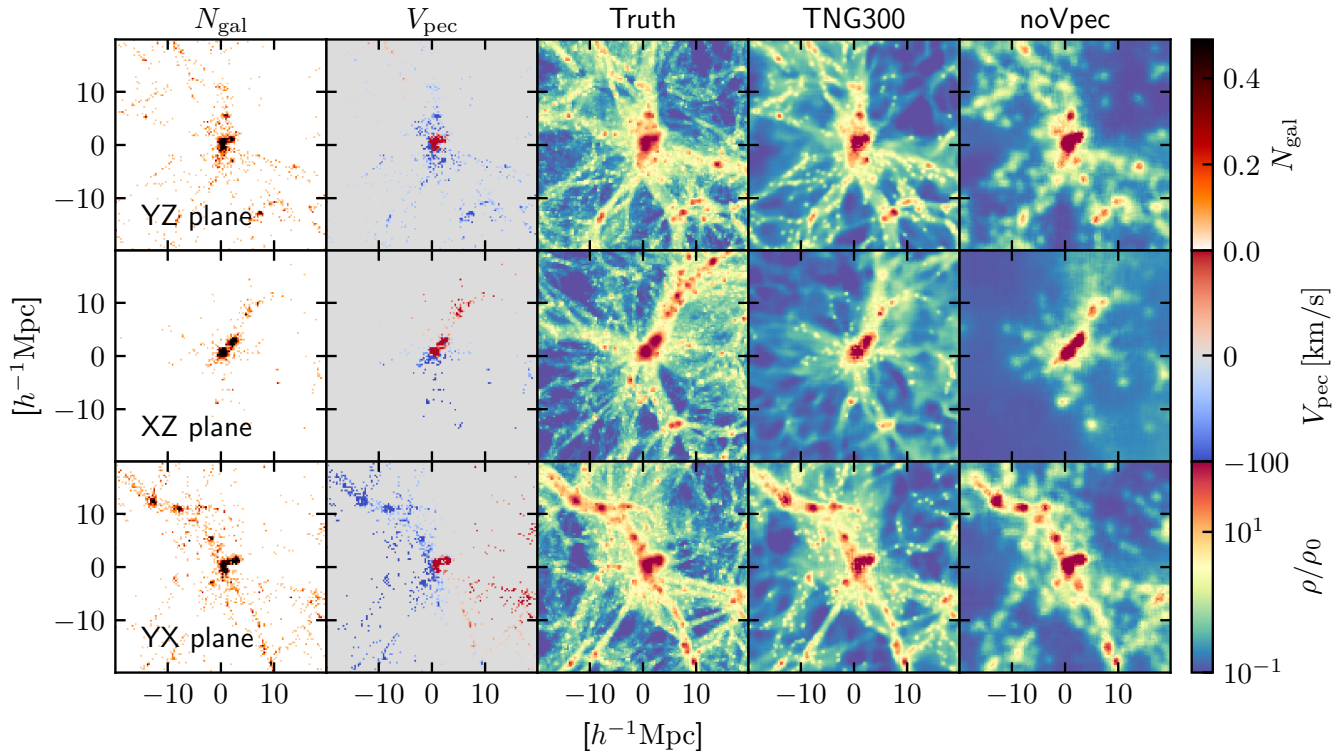


Figure 4. 3-way projections of a single TNG300 validation sample with $5 \text{ Mpc}/h$ -thickness. From left to right: galaxy number (N_{gal}), radial peculiar velocity (V_{pec}), truth dark-matter density (ρ_{truth}), reconstructed dark-matter density (ρ_{TNG300}), and another reconstruction from the CNN architecture without using the radial peculiar velocity (noVpec; ρ_{noVpec}). TNG300 can well reconstruct the filamentary structure of a few-Mpc scales in the true dark-matter distribution, while noVpec does not show such structure.

significant role in reconstructing the small-scale filamentary structure.

4.2. Three-dimensional view of the Local Cosmic Web

Figure 6 shows a sliced view of the reconstructed Cosmic Web integrated over $4 \text{ Mpc}/h$ thickness. Each panel shows the Cosmic Web on the plane of the Supergalactic Cartesian coordinates (SGX, SGY, and SGZ), extended to the full cube with the side length of $40 \text{ Mpc}/h$. Figure 6 clearly shows known local objects that we designated by their common name. The figure also recovers known local large-scale structures. For example, we find a $10 \text{ Mpc}/h$ -spread along $+SGY$ -direction in the SGZ-SGY (upper left panel) and SGY-SGX (lower-right panel) planes. This structure is known as Local Sheet, which connects the Local Group and Virgo cluster and contains M81, NGC5194, Canes II, and Coma I groups (Tully et al. 2008; Courtois et al. 2013). We also find that, around the Local Group, the Local Sheet is connected to the Fornax Wall (Fairall et al. 1994), which is a $20 \text{ Mpc}/h$ -sized spread along $(-SGY, -SGZ)$ -direction, containing Fornax cluster, Eridanus cluster, and Dorado group as members (upper-left panel). At the opposite direction to the Fornax Wall on the SGZ-SGY plane, the

Local Void (Tully & Fisher 1987) is also apparent (also shown on the SGZ-SGX plane), which might extend beyond the boundary of our local universe sample. In Figure 6, we also present the velocity flow lines derived from the reconstructed gravitational potential gradient with arrows and black lines. The velocity flow shows the motion of material from the Local Void to nearby filamentary structures and clusters such as the Local Sheet, Fornax Wall, and Virgo cluster. Note that we cannot reproduce the velocity flow from the Virgo cluster to the Great Attractor ($+SGX$ -direction), because of the limited extension of the volume that we analyze here. However, we would like to emphasize that the recovered dark-matter map provides us detailed density and velocity fields around these known local large-scale structures.

The recovered Cosmic Web also shows a hint of new structures that require further investigation. For example, the direction of the Local Sheet is similar to the direction of the so-called vast polar structure (VPOS), which consists of satellite galaxies, globular clusters and stellar streams around the Milky-way galaxy (Pawlowski et al. 2012). As shown in Figure 6, the Local Sheet, be-

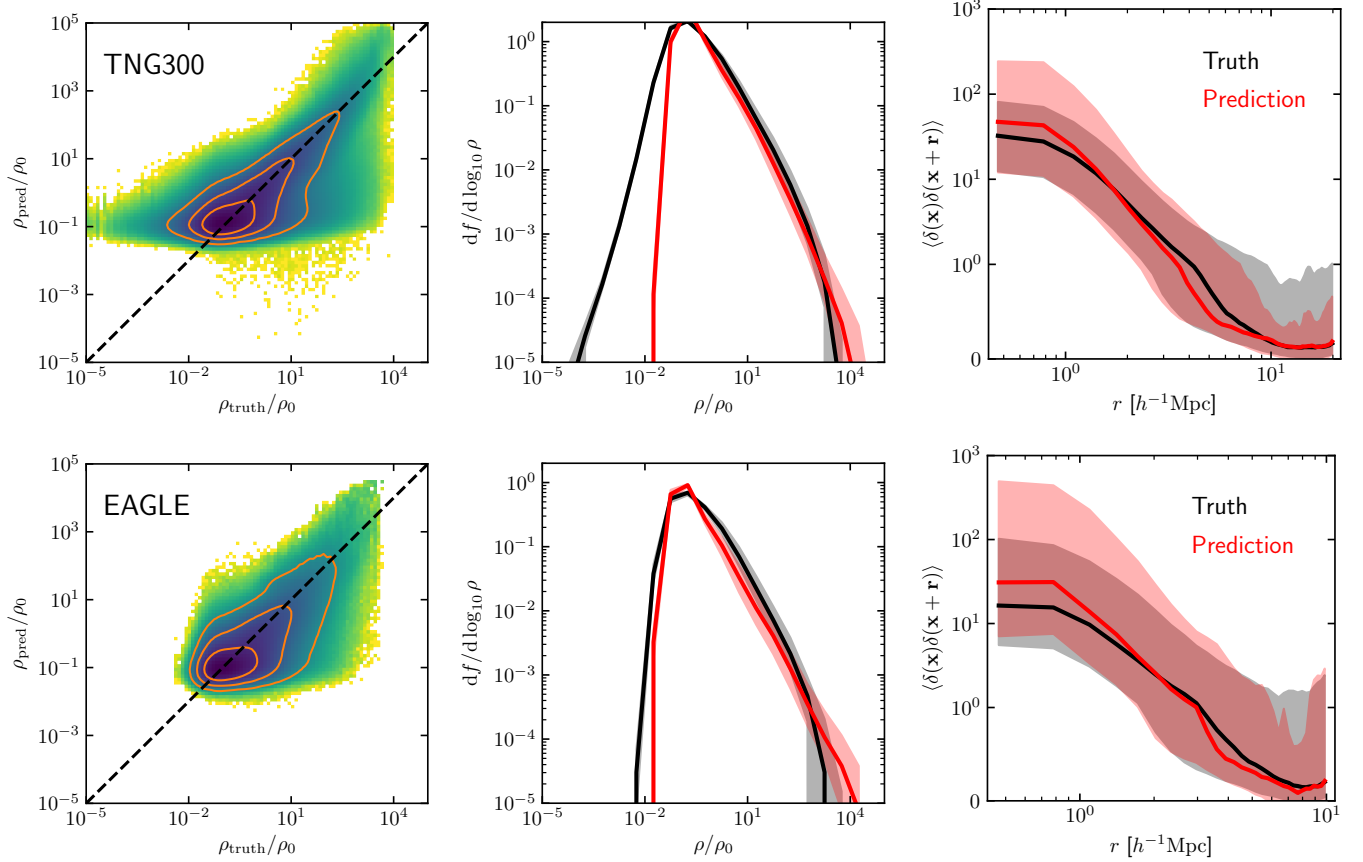


Figure 5. Result of the performance tests for the deep learning result using the three-dimensional dark-matter density field of simulations. Top panel: statistical comparison between the ground truth and the predicted dark-matter density from the entire TNG300 validation sample. From left to right: joint probability distribution (colors) with 1, 2, 3- σ certainty level contours (lines), median (lines) and 1- σ deviation (shades) of histograms, and median (lines) and 1- σ deviation (shades) of the two-point correlation functions. Bottom panel: similar to the top panel, but by applying the TNG100 training to the entire EAGLE test sample.

ing the strongest filamentary structure around the Local Group, is a source of velocity flow; that might cause a connection between the two. Also, a couple of small filaments are visible in our maps, which could be good targets for systematic examination with deep imaging surveys.

Furthermore, to estimate the uncertainties of the dark-matter map, we perform a stress test on our CNN models by incorporating distance measurement uncertainties in the CF3. We use the one standard deviation uncertainty in distance modulus (ϵ_μ) in the CF3,

$$\epsilon_\mu \equiv \sqrt{\frac{1}{\sum_i 1/\epsilon_i^2}}. \quad (15)$$

Here ϵ_i includes the one standard deviation uncertainty determined from a recalibration of galaxy magnitude with H I linewidth (Tully & Courtois 2012), distance measurement of the Tip of the Red Giant Branch from the *Hubble Space Telescope*, Type Ia supernovae from

various samples (Tully et al. 2013), Tully-Fisher relation using *Spitzer* [3.6] photometry, and the Fundamental Plane relation from the *Six Degree Field Galaxy Survey* (6dFGS) (Tully et al. 2016). We then generate 1,000 sets of random distance moduli that follow the normal distribution,

$$P(\Delta\mu) = \frac{1}{\epsilon_\mu \sqrt{2\pi}} \exp\left[-\frac{\Delta\mu^2}{2\epsilon_\mu^2}\right]. \quad (16)$$

Then, we re-calculate the radial peculiar velocity by subtracting the Hubble flow corresponding to the random distances from the V_{GSR} . Since the distance measurement error exists only along the radial direction, we have generated the two-dimensional column density map of the dark matter that is less affected by the error than the three-dimensional dark-matter density field (see Figure 9). Also, we find that the dark-matter column density map driven from TNG300 shows significantly less deviation than that of TNG100, which suf-

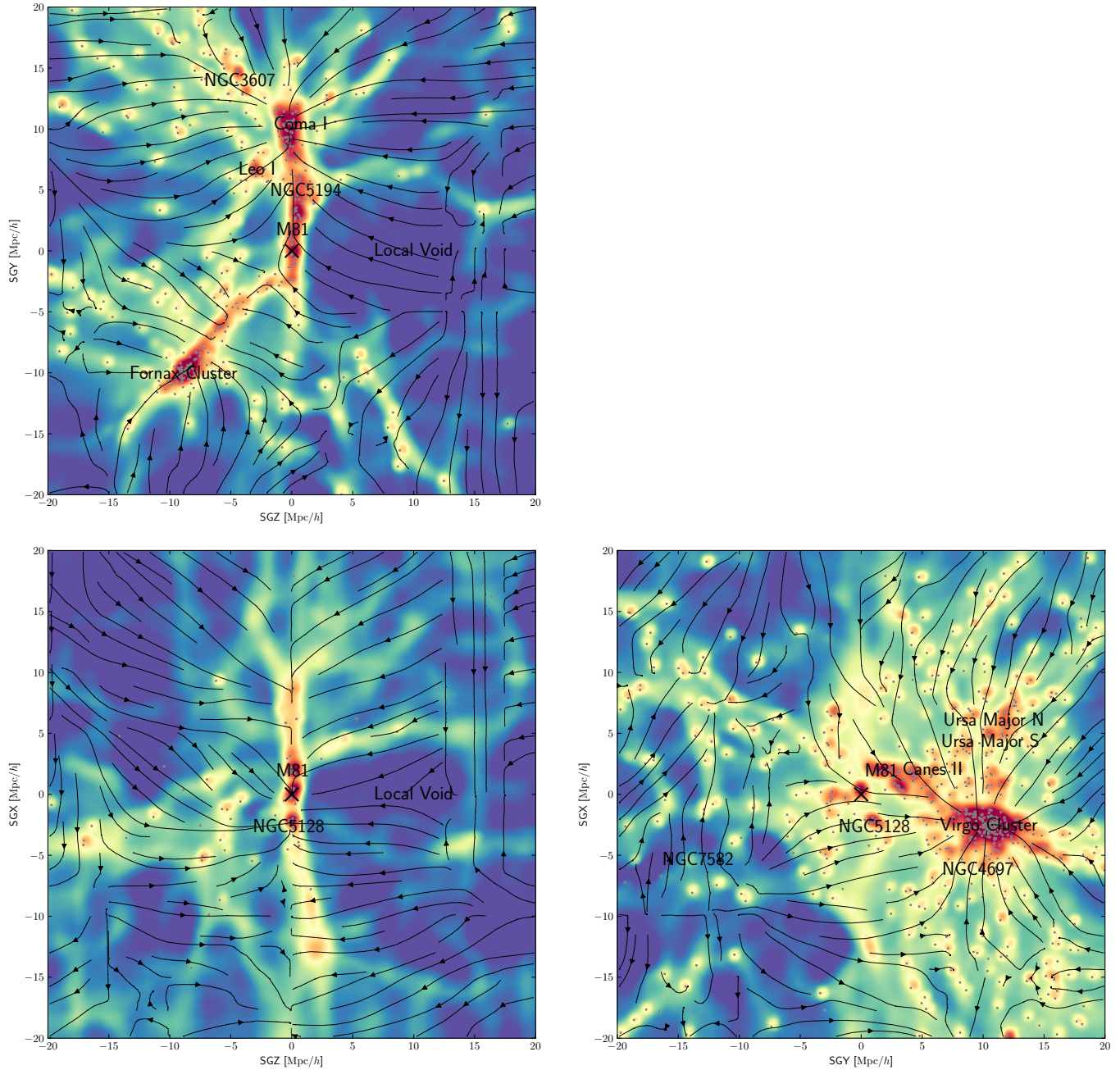


Figure 6. Three-dimensional density maps of the local dark matter with $40 \text{ Mpc}/h$ -boxsize and $4 \text{ Mpc}/h$ -thickness. ‘X’-mark at the center: Milky-way galaxy. Dots: galaxies with $M_B < -15$. Texts: galaxy groups, clusters, and local structures. Arrows: estimated directions of motion derived from the gradient of the reconstructed gravitational potential.

fers from some spurious structure consistently appearing near the Galactic plane.

4.3. Sky map of the Local Cosmic Web

The left panels of Figure 7 (labeled as TNG300) show the recovered local dark-matter map on the sky (gray map),

$$\Sigma(\boldsymbol{\theta}) \equiv \int dr \rho(\boldsymbol{\theta}, r), \quad (17)$$

where $\boldsymbol{\theta}$, r , $\rho(\boldsymbol{\theta}, r)$ are the two-dimensional sky coordinates, distance from the observer, and the dark-matter density at the given $(\boldsymbol{\theta}, r)$, respectively. We use the *Healpix* (Zonca et al. 2019; Górski et al. 2005) package to reconstruct the two-dimensional sky map from the three-dimensional data cube. We set the resolution parameter $N_{\text{side}} = 128$, which roughly corresponds to the angular resolution of $27'$. This figure also shows the locations and radial peculiar velocities of galaxies that

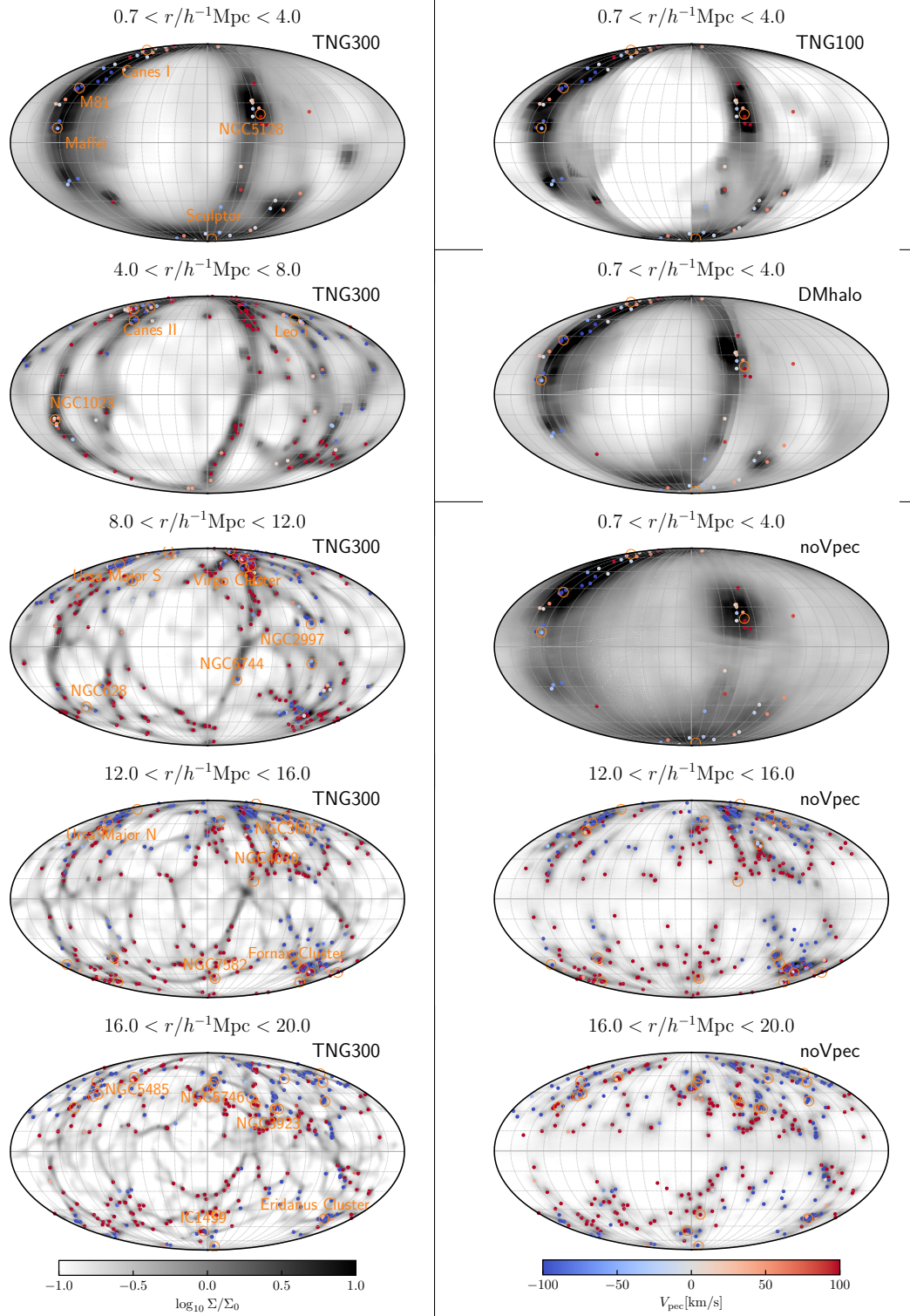


Figure 7. Two-dimensional full-sky map of the local dark-matter column density with $4 \text{ Mpc}/h$ widths. Left panels: predictions from TNG300 training, from the nearest to the farthest radial bin. Right panels: comparison predictions from TNG100 training (TNG100), training with dark matter halos from the dark matter-only simulation (DMhalo), and training without using the radial peculiar velocity (noVpec). Small dots: positions and peculiar velocity (color) of known local galaxies. Large dots: galaxy groups and clusters with their names.

we use for the reconstruction (color-coded dots), as well as the locations of some well-known galaxy groups and clusters (large dots).

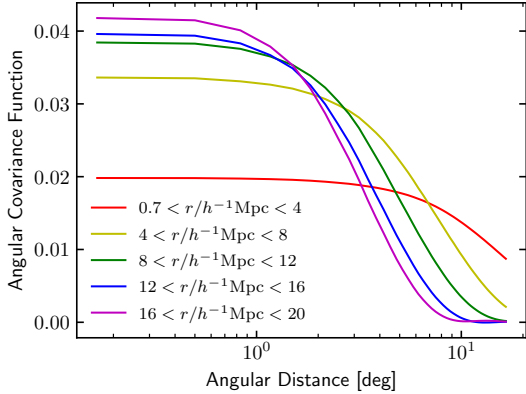


Figure 8. Angular covariance function $C(\delta\theta)$ as a function of angular distance ($\delta\theta$) in the sky. Each angular covariance function roughly follows $C(\delta\theta) \propto \exp(-\delta\theta/\delta\theta_0)$, where $\delta\theta_0$ is a proxy of angular resolution of a degraded map each of whose pixel is statistically independent.

The map in Figure 7 uses the radial distance and radial peculiar velocities reported in the *Cosmicflows-3* catalog (Tully et al. 2016). We have mitigated the 10 – 30% uncertainties of distance measurement in the catalog by adopting the radial binning of $\Delta r = 4 \text{ Mpc}/h$. We further analyze the statistical uncertainties of the recovered dark-matter map by generating 1,000 realizations incorporating the uncertainties of the distance measurement (see Section 4.2). From the high angular resolution map ($N_{\text{side}} = 128$), we define the angular covariance function,

$$C(\delta\theta) \equiv \frac{\langle \delta\Sigma(\boldsymbol{\theta}) \delta\Sigma(\boldsymbol{\theta}') \rangle_{N, \boldsymbol{\theta}, \boldsymbol{\theta}'}}{\Sigma_0^2}, \quad (18)$$

where $\Sigma_0 = \rho_0 \Delta r$ is the mean dark-matter column density, $\langle \dots \rangle_{N, \boldsymbol{\theta}, \boldsymbol{\theta}'}$ is the average over $N = 1,000$ realizations and sky coordinates $\boldsymbol{\theta}$ and $\boldsymbol{\theta}'$ that satisfy $|\boldsymbol{\theta} - \boldsymbol{\theta}'| = \delta\theta$, and $\delta\Sigma(\boldsymbol{\theta}) \equiv \Sigma(\boldsymbol{\theta}) - \langle \Sigma(\boldsymbol{\theta}) \rangle_N$. We found that the angular covariance function follows an exponential decay over $\delta\theta$,

$$C(\delta\theta) \approx C_0 \exp\left(-\frac{\delta\theta}{\delta\theta_0}\right), \quad (19)$$

and the values of the angular scale that shows a strong pixel-to-pixel correlation are $\delta\theta_0 = 20.7^\circ, 9.71^\circ, 6.53^\circ, 5.04^\circ$, and 4.24° , respectively, from the nearest ($r < 4 \text{ Mpc}/h$) to the farthest ($16 \text{ Mpc}/h < r < 20 \text{ Mpc}/h$) radial bins (see Figure 8). $\delta\theta_0$ at different radial bins correspond to the linear scales $\delta\ell = 0.26, 0.68, 0.92, 1.06$, and $1.18 \text{ Mpc}/h$, respectively. $\delta\ell$ at the nearest

radial bin well represent the spatial resolution of the three-dimensional grid ($0.3215 \text{ Mpc}/h$). On the other hand, $\delta\ell$ at the farthest radial bin may mean a typical scale of the filamentary structure at given radial bin width and galaxy number density. For the statistical analysis, we degrade the angular resolution of each map to $\delta\theta_0$ — $N_{\text{side}} = 4, 8, 8, 16$, and 16 from the nearest to the farthest radial bins—and assume that each pixel in the degraded map is statistically independent.

Figure 9 shows the mean ($\langle \log_{10} \Sigma \rangle$; left panel) and the standard deviation ($\Delta \log_{10} \Sigma$; middle panel) of the logarithm of the local dark-matter column density over 1,000 realizations incorporating the uncertainties of the distance measurement. We find that the standard deviation per pixel stays in the range of $\Delta \log_{10} \Sigma / \Sigma_0 \simeq 0.1 - 0.4$, with only a mild dependence to the density contrast. As a result, the signal-to-noise ratio $\text{SNR} \equiv |\langle \log_{10} \Sigma \rangle| / \Delta \log_{10} \Sigma$ scales almost linearly as the density contrast, reaching up to $\text{SNR} \simeq 10$ for the density peaks. On average, the signal-to-noise ratios for dark-matter distribution per pixel at higher Galactic latitudes ($|b| > 10^\circ$) are 4.25, 3.76, 3.94, 4.19, and 4.52, respectively, from the nearest to the farthest radial bin.

Note that, in addition to the distance measurement uncertainty, there are systematic uncertainties in DL mapping itself into the error budget. For example, the galaxy simulations with different resolutions or different sub-grid prescriptions can lead to different DL mapping. We check such systematic effect by comparing TNG300 with various comparison models, including those already introduced in Table 1. To do this, we calculate the on-sky average of the systematics

$$\Delta_{\text{sys}} \equiv \frac{|\log_{10} \Sigma - \log_{10} \Sigma_{\text{TNG300}}|}{\Delta \log_{10} \Sigma_{\text{TNG300}}}, \quad (20)$$

where Σ and Σ_{TNG300} are the local dark-matter column densities from a given comparison model and TNG300, both by adopting the reported values of galaxy locations and peculiar velocities. First, we check the systematic effect of the resolution by comparing the local dark-matter map estimated from TNG100 and TNG300. The top-right panel of Figure 7 shows the $r < 4 \text{ Mpc}/h$ bin dark-matter map driven from the high-resolution result (TNG100). TNG100 systematically underestimate the density contrast by $\Delta_{\text{sys}} = 2.3$ on average (see Table 3).

Secondly, to estimate the systematic effect from different sub-grid prescriptions, we have repeated the deep-learning procedure by using the dark-matter halo samples from the dark-matter-only simulation TNG300-1-Dark by matching the galaxy/halo number density

Table 3. On-sky average (median and 1- σ certainty level in the parenthesis) of the systematics $\Delta_{\text{sys}} \equiv |\log_{10} \Sigma - \log_{10} \Sigma_{\text{TNG300,face}}| / \Delta \log_{10} \Sigma_{\text{TNG300}}$ over high Galactic latitude $|b| > 10^\circ$ with different radial bins. See Table 1 for the definition of each comparison model except TNG100.

Comparison Model	0.7 – 4 Mpc/h	4 – 8 Mpc/h	8 – 12 Mpc/h	12 – 16 Mpc/h	16 – 20 Mpc/h
TNG100	2.281 (1.837 ^{+1.993} _{-1.104})	1.474 (1.196 ^{+1.414} _{-0.842})	-	-	-
diffH0	0.212 (0.171 ^{+0.223} _{-0.115})	0.162 (0.133 ^{+0.148} _{-0.092})	0.154 (0.116 ^{+0.161} _{-0.083})	0.152 (0.117 ^{+0.153} _{-0.082})	0.160 (0.128 ^{+0.151} _{-0.092})
16mag	1.032 (0.949 ^{+0.748} _{-0.647})	1.093 (0.868 ^{+1.089} _{-0.611})	0.862 (0.716 ^{+0.729} _{-0.508})	0.785 (0.641 ^{+0.751} _{-0.455})	0.804 (0.631 ^{+0.790} _{-0.443})
17mag	1.178 (0.901 ^{+1.081} _{-0.572})	1.105 (0.889 ^{+1.026} _{-0.621})	1.001 (0.815 ^{+0.947} _{-0.575})	0.887 (0.726 ^{+0.862} _{-0.502})	0.898 (0.734 ^{+0.833} _{-0.506})
noVpec	1.935 (1.715 ^{+1.919} _{-1.359})	1.105 (0.834 ^{+1.120} _{-0.631})	0.943 (0.701 ^{+0.890} _{-0.524})	0.828 (0.672 ^{+0.751} _{-0.470})	0.750 (0.626 ^{+0.742} _{-0.440})
stellarMass	1.544 (1.256 ^{+1.435} _{-0.843})	1.175 (0.946 ^{+1.156} _{-0.684})	0.925 (0.734 ^{+0.909} _{-0.521})	0.877 (0.692 ^{+0.837} _{-0.485})	0.907 (0.713 ^{+0.899} _{-0.490})
DMhalo	1.737 (1.154 ^{+2.253} _{-0.863})	1.445 (1.127 ^{+1.414} _{-0.816})	1.176 (0.913 ^{+1.097} _{-0.610})	1.057 (0.846 ^{+1.029} _{-0.595})	0.957 (0.796 ^{+0.889} _{-0.574})

(DMhalo). The right panels of Figure 9 show the difference between the two dark-matter maps in units of standard deviation at each pixel. Even with this extreme comparison between full hydrodynamic simulation and pure N -body simulation, we find that systematic effects lead to $\Delta_{\text{sys}} = 1.7, 1.4, 1.2, 1.1,$ and 1.0 on average from the top (nearest) to the bottom (furthest) maps.

We further test the systematic effect due to different Hubble parameters ($H_0 = 75$ km/s/Mpc; diffH0) and find only $\Delta_{\text{sys}} \simeq 0.15$. Different B -band magnitude cuts ($M_B < -16$ and -17 ; 16mag and 17mag, respectively) and using total stellar mass instead of galaxy number (stellarMass) lead to $\Delta_{\text{sys}} \simeq 1$. Most importantly, none of the systematic maps shows a significant correlation with the derived cosmic web structure, ensuring the robustness of the derived dark-matter distribution, or the Cosmic Web (see the right panel of Figure 9).

The most striking feature that we have recovered in this study is the filamentary Cosmic Web that is apparent in Figures 7 and 9. First of all, we find that the radial peculiar velocity information is vital to reconstructing the cosmic web, without which the same DL algorithm can not reproduce the Cosmic Web structure at all. For example, the right panels in Figure 7, indicated by noVpec, show the deep-learning result only using galaxy distributions. Note the absence of the filamentary structure in those maps. We note that the noVpec maps resemble the smoothed version of the galaxy distribution. The deep-learning algorithm with stellar-mass weighted galaxy distribution, without peculiar velocity information, leads to the similarly poor quality map.

Another interesting feature in the map is the dark-matter distribution at lower Galactic latitudes ($|b| < 10^\circ$) where we do not have any input galaxy data. To our surprise, we find that the averaged signal-to-noise ratios per pixel for this region are 4.18, 4.73, 5.31, 5.80, and 6.21, respectively, from the nearest to the farthest

radial bin. We, however, anticipate that the theoretical uncertainties for the DL mapping would be most substantial for this region. For example, from the aforementioned studies on systematic uncertainties, we find that, on average, lower Galactic latitudes ($|b| < 10^\circ$) map suffers about $\delta\Delta_{\text{sys}} \simeq 0.5$ more systematical shifts than higher Galactic latitudes ($|b| > 10^\circ$) map. This is indicated in the top two panels of Figure 7 and the systematic shifts shown in the right panels of Figure 9.

5. DISCUSSION

In this paper, we present a novel convolutional neural network (CNN)-based deep learning (DL) method of reconstructing the local dark-matter distribution map and discover the local Cosmic-Web structure traced by the positions and radial peculiar velocities of *Cosmicflow-3* galaxies. We find that including the radial peculiar velocity field is the key to recover the dark matter distribution in the Cosmic Web. Incorporating the observational uncertainties in the galaxy distance measurements, the average detection significance of the dark-matter map exceeds $4.1\text{-}\sigma$ for each *Healpix* pixel at higher Galactic latitudes ($|b| > 10^\circ$). The quoted statistical significance, however, does not include the uncertainties in the galaxy-to-dark-matter mapping itself. We have tested that the DL results stay robustly for three different simulations: TNG100-1 and TNG300-1 from the *Illustris-TNG* simulation and RefL0100N1504 from the *EAGLE* simulation, but future studies must quantify the theoretical uncertainties by applying the same method to the large-scale structure simulations with different baryonic prescriptions. The comparison of the DL results between TNG300-1 and N -body simulations, however, indicates that the filamentary Cosmic-Web structure may not suffer from the systematic effects.

The main statistical uncertainty in the galaxy data comes from the uncertainty in the distance measurement. As the observed shift in the galaxy spectra con-

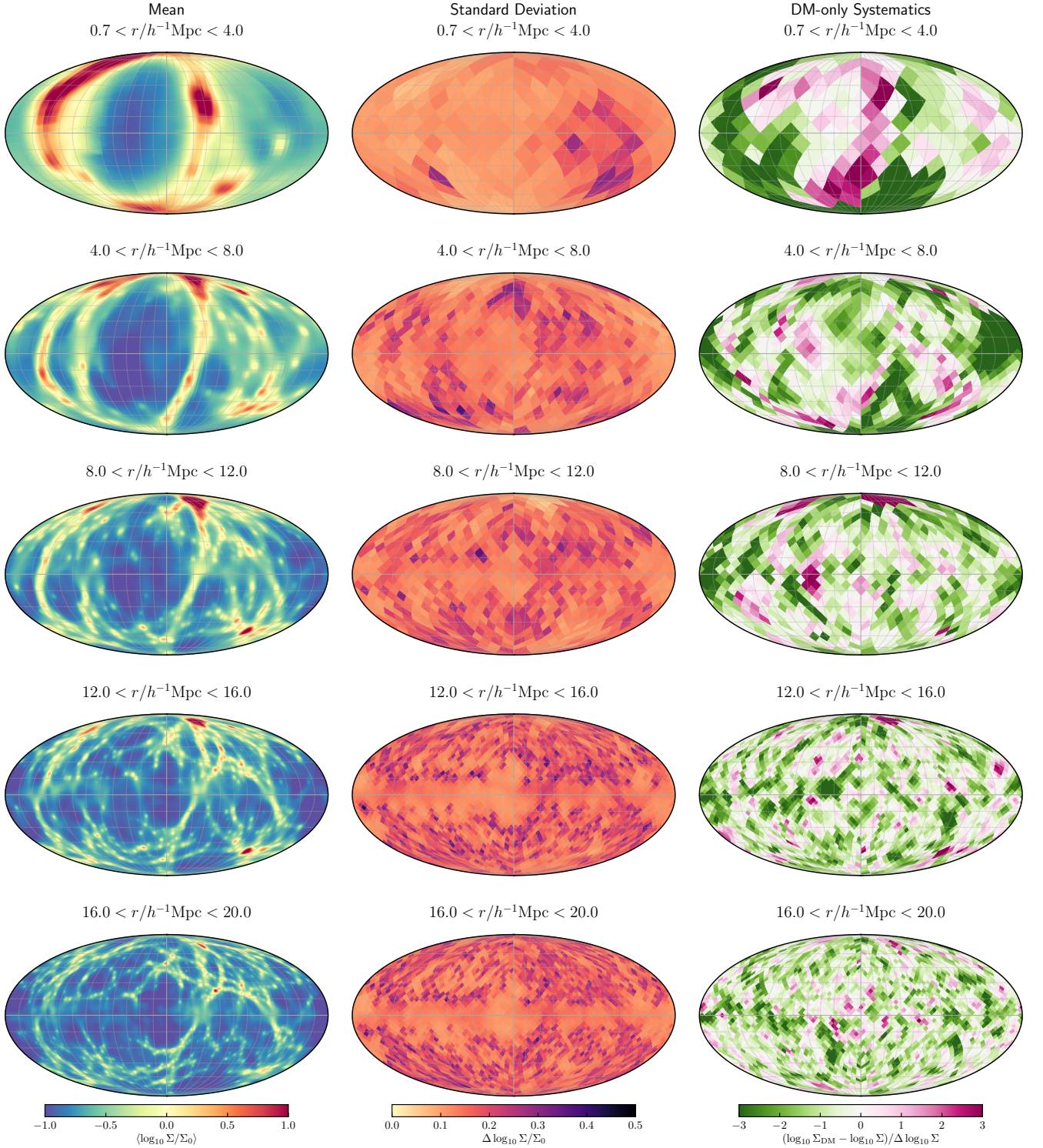


Figure 9. Same as Figure 7, but showing statistical maps. Left panels: mean of the logarithm of dark-matter column-density estimated from 1000 random realizations incorporating the uncertainties in distance estimate to the local galaxies. Middle panels: standard deviation from 1,000 random realizations ($N_{\text{side}} = 4, 8, 8, 16, 16$ from top to bottom). Right panels: systematic bias from different simulation input for the deep-learning (TNG300 vs. DMhalo).

strains the sum of the distance (Hubble flow) and the radial peculiar velocity, the uncertainty affects both the galaxy distribution and the radial peculiar velocity field. Therefore, to obtain a dark-matter map with higher significance, it is necessary to explore the ways to reduce the uncertainties of the current distance estimators such as the Tip of the Red Giant Branch, the Type Ia supernova, and the Fundamental Plane through continuous cross-calibration (Tully et al. 2016), and to increase the number of galaxies with measured distances through systematic surveys (e.g., *6dFGS* (Springob et al. 2014), *James Webb Space Telescope* (Gardner et al. 2006)).

We anticipate that the reconstructed three-dimensional dark-matter map and peculiar velocity field will open an entirely new chapter of cosmological study. For example, the dark-matter map can make it possible to run the cosmological galaxy simulations with the *precise* initial condition of the Local Group for studying the past and future of our cosmic neighborhood. It will also allow the in-depth study of the nature of dark matter by cross-correlating the reconstructed dark matter map with the full-sky diffuse emission maps constructed from the radio-to-gamma-ray electromagnetic spectra as well as the full-sky map of gravitational wave binaries. The latter can test the models where black holes in binaries have formed out of dark matter (Shandera et al. 2018).

Finally, as we have introduced a novel CNN-based DL method to reconstruct the local Cosmic Web, the quantitative study comparing the prediction power of the DL method presented here with pre-existing methods such as BORG may be in order. Note that, however, many previous studies reconstruct the dark matter distribution on scales much larger than the size of our local Cosmic Web (e.g., $\gtrsim 3 - 5 \text{ Mpc}/h$ in Jasche & Wandelt 2013; Jasche et al. 2015), which complicates the direct comparison between the two methods. Nevertheless, an

additional study that applies the existing methods to similar observational and simulation data to ours and compares them to our DL method would be beneficial, and we leave it for the future.

ACKNOWLEDGMENTS

Authors acknowledge Christophe Pichon, Changbom Park, Sungryong Hong, Inkyu Park, Dongsu Bak, Graziano Rossi, and Yung-Kyun Noh for discussion. Authors also acknowledge an anonymous referee for suggestions to improve this article. The list of nearby galaxy groups and clusters is derived from www.atlasoftheuniverse.com. Authors acknowledge the Korea Institute for Advanced Study for providing computing resources (KIAS Center for Advanced Computation Linux Cluster System). Computational data were transferred through a high-speed network provided by the Korea Research Environment Open NETwork (KRE-ONET).

SEH was partly supported by Basic Science Research Program through the National Research Foundation of Korea funded by the Ministry of Education (2018R1A6-A1A06024977). SEH was also partly supported by the project 우주 거대구조를 이용한 암흑우주 연구 (“Understanding Dark Universe Using Large Scale Structure of the Universe”), funded by the Ministry of Science. DJ was supported at Pennsylvania State University by NSF grant (AST-1517363) and NASA ATP program (80NSSC18K1103). JK was supported by a KIAS Individual Grant (KG039603) via the Center for Advanced Computation at Korea Institute for Advanced Study.

Software: HEALPix (Górski et al. 2005), Healpy (Zonca et al. 2019), astropy (Astropy Collaboration et al. 2013, 2018), NumPy (Van Der Walt et al. 2011; Harris et al. 2020), Scipy (Jones et al. 2001; Virtanen et al. 2020), matplotlib (Hunter 2007), pandas (Wes McKinney 2010), Keras (Chollet et al. 2015), Tensorflow backend (Abadi et al. 2015)

REFERENCES

- Aaronson, M. 1983, *The Astrophysical Journal Letter*, 266, L11, doi: [10.1086/183969](https://doi.org/10.1086/183969)
- Aartsen, M. G., Ackermann, M., Adams, J., et al. 2018, *Eur. Phys. J. C*, 78, 831, doi: [10.1140/epjc/s10052-018-6273-3](https://doi.org/10.1140/epjc/s10052-018-6273-3)
- Abadi, M., Agarwal, A., Barham, P., et al. 2015, *TensorFlow: Large-Scale Machine Learning on Heterogeneous Systems*. <https://www.tensorflow.org/>
- Abbott, T. M. C., Abdalla, F. B., Alarcon, A., et al. 2018, *Physical Review D*, 98, 043526, doi: [10.1103/PhysRevD.98.043526](https://doi.org/10.1103/PhysRevD.98.043526)
- Ackermann, M., Albert, A., Anderson, B., et al. 2015, *Physical Review Letter*, 115, 231301, doi: [10.1103/PhysRevLett.115.231301](https://doi.org/10.1103/PhysRevLett.115.231301)
- Akerib, D. S., Alsum, S., Araújo, H. M., et al. 2017, *Physical Review Letter*, 118, 021303, doi: [10.1103/PhysRevLett.118.021303](https://doi.org/10.1103/PhysRevLett.118.021303)

- Ammazzalorso, S., Gruen, D., Regis, M., et al. 2020, *Physical Review Letter*, 124, 101102, doi: [10.1103/PhysRevLett.124.101102](https://doi.org/10.1103/PhysRevLett.124.101102)
- Anderson, L., Aubourg, É., Bailey, S., et al. 2014, *Monthly Notices of the Royal Astronomical Society*, 441, 24, doi: [10.1093/mnras/stu523](https://doi.org/10.1093/mnras/stu523)
- Arcadi, G., Dutra, M., Ghosh, P., et al. 2018, *Eur. Phys. J. C*, 78, 203, doi: [10.1140/epjc/s10052-018-5662-y](https://doi.org/10.1140/epjc/s10052-018-5662-y)
- Astropy Collaboration, Robitaille, T. P., Tollerud, E. J., et al. 2013, *Astronomy & Astrophysics*, 558, A33, doi: [10.1051/0004-6361/201322068](https://doi.org/10.1051/0004-6361/201322068)
- Astropy Collaboration, Price-Whelan, A. M., SipHocz, B. M., et al. 2018, *aj*, 156, 123, doi: [10.3847/1538-3881/aabc4f](https://doi.org/10.3847/1538-3881/aabc4f)
- Atlas Collaboration. 2019, *Journal of High Energy Physics*, 2019, 142, doi: [10.1007/JHEP05\(2019\)142](https://doi.org/10.1007/JHEP05(2019)142)
- Bell, E. F., McIntosh, D. H., Katz, N., & Weinberg, M. D. 2003, *The Astrophysical Journal Supplement Series*, 149, 289, doi: [10.1086/378847](https://doi.org/10.1086/378847)
- Camps, P., Trčka, A., Trayford, J., et al. 2018, *The Astrophysical Journal Supplement Series*, 234, 20, doi: [10.3847/1538-4365/aaa24c](https://doi.org/10.3847/1538-4365/aaa24c)
- Carlesi, E., Sorce, J. G., Hoffman, Y., et al. 2016, *Monthly Notices of the Royal Astronomical Society*, 458, 900, doi: [10.1093/mnras/stw357](https://doi.org/10.1093/mnras/stw357)
- Carrick, J., Turnbull, S. J., Lavaux, G., & Hudson, M. J. 2015, *Monthly Notices of the Royal Astronomical Society*, 450, 317, doi: [10.1093/mnras/stv547](https://doi.org/10.1093/mnras/stv547)
- Chollet, F., et al. 2015, *Keras*, <https://keras.io>
- Clowe, D., Bradač, M., Gonzalez, A. H., et al. 2006, *The Astrophysical Journal Letter*, 648, L109, doi: [10.1086/508162](https://doi.org/10.1086/508162)
- Cooke, R. J., Pettini, M., Jorgenson, R. A., Murphy, M. T., & Steidel, C. C. 2014, *The Astrophysical Journal*, 781, 31, doi: [10.1088/0004-637x/781/1/31](https://doi.org/10.1088/0004-637x/781/1/31)
- Courtois, H. M., Pomarède, D., Tully, R. B., Hoffman, Y., & Courtois, D. 2013, *The Astronomical Journal*, 146, 69, doi: [10.1088/0004-6256/146/3/69](https://doi.org/10.1088/0004-6256/146/3/69)
- Crain, R. A., Schaye, J., Bower, R. G., et al. 2015, *Monthly Notices of the Royal Astronomical Society*, 450, 1937, doi: [10.1093/mnras/stv725](https://doi.org/10.1093/mnras/stv725)
- Davis, M., Efstathiou, G., Frenk, C. S., & White, S. D. M. 1985, *The Astrophysical Journal*, 292, 371, doi: [10.1086/163168](https://doi.org/10.1086/163168)
- Desjacques, V., Jeong, D., & Schmidt, F. 2018, *Physics Reports*, 733, 1, doi: [10.1016/j.physrep.2017.12.002](https://doi.org/10.1016/j.physrep.2017.12.002)
- Fairall, A. P., Paverd, W. R., & Ashley, R. P. 1994, in *Astronomical Society of the Pacific Conference Series*, Vol. 67, *Unveiling Large-Scale Structures Behind the Milky Way*, ed. C. Balkowski & R. C. Kraan-Korteweg, 21
- Fang, K., Banerjee, A., Charles, E., & Omori, Y. 2020, arXiv e-prints, arXiv:2002.06234. <https://arxiv.org/abs/2002.06234>
- Fornasa, M., Cuoco, A., Zavala, J., et al. 2016, *Physical Review D*, 94, 123005, doi: [10.1103/PhysRevD.94.123005](https://doi.org/10.1103/PhysRevD.94.123005)
- Gardner, J. P., Mather, J. C., Clampin, M., et al. 2006, *Space Science Reviews*, 123, 485, doi: [10.1007/s11214-006-8315-7](https://doi.org/10.1007/s11214-006-8315-7)
- Giesen, G., Boudaud, M., Génolini, Y., et al. 2015, *Journal of Cosmology and Astroparticle Physics*, 2015, 023, doi: [10.1088/1475-7516/2015/09/023](https://doi.org/10.1088/1475-7516/2015/09/023)
- Glorot, X., Bordes, A., & Bengio, Y. 2011, in *Proceedings of the fourteenth international conference on artificial intelligence and statistics*, 315–323
- Górski, K. M., Hivon, E., Banday, A. J., et al. 2005, *The Astrophysical Journal*, 622, 759, doi: [10.1086/427976](https://doi.org/10.1086/427976)
- Gottloeber, S., Hoffman, Y., & Yepes, G. 2010, arXiv e-prints, arXiv:1005.2687. <https://arxiv.org/abs/1005.2687>
- Hahnloser, R. H. R., Sarpeshkar, R., Mahowald, M. A., Douglas, R. J., & Seung, H. S. 2000, *Nature*, 405, 947, doi: [10.1038/35016072](https://doi.org/10.1038/35016072)
- Harris, C. R., Millman, K. J., van der Walt, S. J., et al. 2020, *Nature*, 585, 357, doi: [10.1038/s41586-020-2649-2](https://doi.org/10.1038/s41586-020-2649-2)
- Huchra, J. P., Macri, L. M., Masters, K. L., et al. 2012, *The Astrophysical Journal Supplement Series*, 199, 26, doi: [10.1088/0067-0049/199/2/26](https://doi.org/10.1088/0067-0049/199/2/26)
- Hunter, J. D. 2007, *Computing in Science Engineering*, 9, 90, doi: [10.1109/MCSE.2007.55](https://doi.org/10.1109/MCSE.2007.55)
- Ioffe, S., & Szegedy, C. 2015, arXiv e-prints, arXiv:1502.03167. <https://arxiv.org/abs/1502.03167>
- Jasche, J., Leclercq, F., & Wandelt, B. D. 2015, *Journal of Cosmology and Astroparticle Physics*, 2015, 036, doi: [10.1088/1475-7516/2015/01/036](https://doi.org/10.1088/1475-7516/2015/01/036)
- Jasche, J., & Wandelt, B. D. 2013, *Monthly Notices of the Royal Astronomical Society*, 432, 894, doi: [10.1093/mnras/stt449](https://doi.org/10.1093/mnras/stt449)
- Jeffrey, N., Lanusse, F., Lahav, O., & Starck, J.-L. 2020, *Monthly Notices of the Royal Astronomical Society*, 492, 5023, doi: [10.1093/mnras/staa127](https://doi.org/10.1093/mnras/staa127)
- Jones, E., Oliphant, T., Peterson, P., et al. 2001
- Kingma, D. P., & Ba, J. 2014, arXiv e-prints, arXiv:1412.6980. <https://arxiv.org/abs/1412.6980>

- Kourkchi, E., Courtois, H. M., Graziani, R., et al. 2020, *The Astronomical Journal*, 159, 67, doi: [10.3847/1538-3881/ab620e](https://doi.org/10.3847/1538-3881/ab620e)
- Larson, D., Dunkley, J., Hinshaw, G., et al. 2011, *The Astrophysical Journal Supplement Series*, 192, 16, doi: [10.1088/0067-0049/192/2/16](https://doi.org/10.1088/0067-0049/192/2/16)
- Lavaux, G., & Hudson, M. J. 2011, *Monthly Notices of the Royal Astronomical Society*, 416, 2840, doi: [10.1111/j.1365-2966.2011.19233.x](https://doi.org/10.1111/j.1365-2966.2011.19233.x)
- Lavaux, G., & Jasche, J. 2016, *Monthly Notices of the Royal Astronomical Society*, 455, 3169, doi: [10.1093/mnras/stv2499](https://doi.org/10.1093/mnras/stv2499)
- Libeskind, N. I., Yepes, G., Knebe, A., et al. 2010, *Monthly Notices of the Royal Astronomical Society*, 401, 1889, doi: [10.1111/j.1365-2966.2009.15766.x](https://doi.org/10.1111/j.1365-2966.2009.15766.x)
- Licquia, T. C., & Newman, J. A. 2015, *The Astrophysical Journal*, 806, 96, doi: [10.1088/0004-637X/806/1/96](https://doi.org/10.1088/0004-637X/806/1/96)
- Marinacci, F., Vogelsberger, M., Pakmor, R., et al. 2018, *Monthly Notices of the Royal Astronomical Society*, 480, 5113, doi: [10.1093/mnras/sty2206](https://doi.org/10.1093/mnras/sty2206)
- Milletari, F., Navab, N., & Ahmadi, S.-A. 2016, arXiv e-prints, arXiv:1606.04797. <https://arxiv.org/abs/1606.04797>
- Modi, C., Feng, Y., & Seljak, U. 2018, *Journal of Cosmology and Astroparticle Physics*, 2018, 028, doi: [10.1088/1475-7516/2018/10/028](https://doi.org/10.1088/1475-7516/2018/10/028)
- Naiman, J. P., Pillepich, A., Springel, V., et al. 2018, *Monthly Notices of the Royal Astronomical Society*, 477, 1206, doi: [10.1093/mnras/sty618](https://doi.org/10.1093/mnras/sty618)
- Nelson, D., Pillepich, A., Springel, V., et al. 2018, *Monthly Notices of the Royal Astronomical Society*, 475, 624, doi: [10.1093/mnras/stx3040](https://doi.org/10.1093/mnras/stx3040)
- Nelson, D., Springel, V., Pillepich, A., et al. 2019, *Computational Astrophysics and Cosmology*, 6, 2, doi: [10.1186/s40668-019-0028-x](https://doi.org/10.1186/s40668-019-0028-x)
- Paturol, G., Petit, C., Prugniel, P., et al. 2003, *Astronomy & Astrophysics*, 412, 45, doi: [10.1051/0004-6361:20031411](https://doi.org/10.1051/0004-6361:20031411)
- Pawlowski, M. S., Pflamm-Altenburg, J., & Kroupa, P. 2012, *Monthly Notices of the Royal Astronomical Society*, 423, 1109, doi: [10.1111/j.1365-2966.2012.20937.x](https://doi.org/10.1111/j.1365-2966.2012.20937.x)
- Pillepich, A., Nelson, D., Hernquist, L., et al. 2018, *Monthly Notices of the Royal Astronomical Society*, 475, 648, doi: [10.1093/mnras/stx3112](https://doi.org/10.1093/mnras/stx3112)
- Planck Collaboration, Aghanim, N., Akrami, Y., et al. 2018, arXiv e-prints, arXiv:1807.06209. <https://arxiv.org/abs/1807.06209>
- Ronneberger, O., Fischer, P., & Brox, T. 2015, arXiv e-prints, arXiv:1505.04597. <https://arxiv.org/abs/1505.04597>
- Rubin, V. C., & Ford, W. Kent, J. 1970, *The Astrophysical Journal*, 159, 379, doi: [10.1086/150317](https://doi.org/10.1086/150317)
- Schaye, J., Crain, R. A., Bower, R. G., et al. 2015, *Monthly Notices of the Royal Astronomical Society*, 446, 521, doi: [10.1093/mnras/stu2058](https://doi.org/10.1093/mnras/stu2058)
- Shandera, S., Jeong, D., & Grasshorn Gebhardt, H. S. 2018, *Physical Review Letter*, 120, 241102, doi: [10.1103/PhysRevLett.120.241102](https://doi.org/10.1103/PhysRevLett.120.241102)
- Shirasaki, M., Yoshida, N., & Ikeda, S. 2019, *Physical Review D*, 100, 043527, doi: [10.1103/PhysRevD.100.043527](https://doi.org/10.1103/PhysRevD.100.043527)
- Smith, L. N. 2015, arXiv e-prints, arXiv:1506.01186. <https://arxiv.org/abs/1506.01186>
- Springel, V., Pakmor, R., Pillepich, A., et al. 2018, *Monthly Notices of the Royal Astronomical Society*, 475, 676, doi: [10.1093/mnras/stx3304](https://doi.org/10.1093/mnras/stx3304)
- Springob, C. M., Magoulas, C., Colless, M., et al. 2014, *Monthly Notices of the Royal Astronomical Society*, 445, 2677, doi: [10.1093/mnras/stu1743](https://doi.org/10.1093/mnras/stu1743)
- Tröster, T., Camera, S., Fornasa, M., et al. 2017, *Monthly Notices of the Royal Astronomical Society*, 467, 2706, doi: [10.1093/mnras/stx365](https://doi.org/10.1093/mnras/stx365)
- Tully, R. B., & Courtois, H. M. 2012, *The Astrophysical Journal*, 749, 78, doi: [10.1088/0004-637X/749/1/78](https://doi.org/10.1088/0004-637X/749/1/78)
- Tully, R. B., Courtois, H. M., & Sorce, J. G. 2016, *The Astronomical Journal*, 152, 50, doi: [10.3847/0004-6256/152/2/50](https://doi.org/10.3847/0004-6256/152/2/50)
- Tully, R. B., & Fisher, J. R. 1987, *Atlas of Nearby Galaxies* (Cambridge University Press)
- Tully, R. B., Shaya, E. J., Karachentsev, I. D., et al. 2008, *The Astrophysical Journal*, 676, 184, doi: [10.1086/527428](https://doi.org/10.1086/527428)
- Tully, R. B., Courtois, H. M., Dolphin, A. E., et al. 2013, *The Astronomical Journal*, 146, 86, doi: [10.1088/0004-6256/146/4/86](https://doi.org/10.1088/0004-6256/146/4/86)
- Van Der Walt, S., Colbert, S. C., & Varoquaux, G. 2011, *Computing in science & engineering*, 13, 22
- Vannerom, D. 2019, *Proc. Sci., DIS2019*, 111, doi: [10.22323/1.352.0111](https://doi.org/10.22323/1.352.0111)
- Virtanen, P., Gommers, R., Oliphant, T. E., et al. 2020, *Nature Methods*, 17, 261, doi: [10.1038/s41592-019-0686-2](https://doi.org/10.1038/s41592-019-0686-2)
- Wes McKinney. 2010, in *Proceedings of the 9th Python in Science Conference*, ed. Stéfan van der Walt & Jarrod Millman, 56 – 61, doi: [10.25080/Majora-92bf1922-00a](https://doi.org/10.25080/Majora-92bf1922-00a)
- Wilman, D. J., & Erwin, P. 2012, *The Astrophysical Journal*, 746, 160, doi: [10.1088/0004-637X/746/2/160](https://doi.org/10.1088/0004-637X/746/2/160)
- Zonca, A., Singer, L., Lenz, D., et al. 2019, *J. Open Sour. Soft.*, 4, 1298, doi: [10.21105/joss.01298](https://doi.org/10.21105/joss.01298)
- Zwicky, F. 1933, *Helv. Phys. Acta*, 6, 110